Science Advances
AAAS

advances.sciencemag.org/cgi/content/full/6/19/eaaz6912/DC1

Supplementary Materials for

Leveraging elastic instabilities for amplified performance: Spine-inspired high-speed and high-force soft robots

Yichao Tang, Yinding Chi, Jiefeng Sun, Tzu-Hao Huang, Omid H. Maghsoudi, Andrew Spence, Jianguo Zhao, Hao Su, Jie Yin*

*Corresponding author. Email: jyin8@ncsu.edu

Published 8 May 2020, *Sci. Adv.* **6**, eaaz6912 (2020)
DOI: 10.1126/sciadv.aaz6912

The PDF file includes:

Supplementary Text
Figs. S1 to S9
Tables S1 to S4
Legends for movies S1 to S9
References

Other Supplementary Material for this manuscript includes the following:

(available at advances.sciencemag.org/cgi/content/full/6/19/eaaz6912/DC1)

Movies S1 to S9

Text

1. Equilibrium Bending Angle of the Bistable Hybrid Soft Bending Actuator (BH-SBA)

After the spring pre-tension release, the BH-SBA reaches the equilibrium with a bending angle of $\theta = \pm\, \theta_{\mathrm{eq}}$, which has a local minimum potential energy U_{eq}. The equilibrium bending angle θ_{eq} can be obtained by minimizing the total potential energy of the bistable actuator system U_{total}. We have

$$U_{total} = U_{actuator} + U_{spring} \tag{S-1}$$

where $U_{actuator}$ is the strain energy in the soft bending actuator and U_{spring} is the potential energy in the spring as below

$$U_{total} = 2\int_L \frac{1}{2} EI\kappa^2 dx + 2\int_V \frac{1}{2} E\varepsilon^2 dV + \frac{1}{2} k\left\{\Delta x_I - L_1\left[1-\cos(\theta/2)\right]\right\}^2 \tag{S-2}$$

where the first and second term represents the bending energy and stretching energy in the soft bending actuator, respectively, and the third term represents the potential energy of the spring at rest state. Here we assume free rotation of the center joint in the rigid spine and uniform curvature in soft actuators. L is the length of the spine, V is the volume of the soft actuator, and L_1 denotes the distance between the anchored points of the spring. k is the stiffness of the spring. Δx_I represents the spring extension at unstable planar state (State I). EI is the bending stiffness of the soft bending actuator with E being Young's modulus of constituent soft material (Ecoflex) and I being the moment of inertia. $\kappa \approx 2\tan\left(\theta/2\right)/L$ is the approximate curvature in the bent soft actuator determined by the bistable mechanism. $\varepsilon \approx 1-\theta/\left[2\tan(\theta/2)\right]$ is the approximate strain in the soft actuator. L_1 denotes the distance between the anchored points of the spring. Detailed geometry and material property can be found in Fig. S1 and Table. S1.

It should be noted that this model is simplified through homogenization without considering its pneumatic channels. We also assume the idealized linear elastic materials behavior in the homogenized continuous layer despite the nonlinear deformation in the elastomer.

θ_{eq} will be obtained by minimizing the total potential energy, i.e.

$$\frac{dU_{total}}{d\theta} = 0 \tag{S-3}$$

The data on the predicted value of θ_{eq} in Fig. 2B is obtained by numerically solving Eq. (S-3).

2. Energy Barrier of the BH-SBA

With Eq. (S-2), the energy barrier ΔE between the unstable state and the equilibrium states can be obtained as:

$$\Delta E = U_I - U_{eq} = \frac{1}{2}kL_1\left[1-\cos(\theta_{eq}/2)\right]\left\{2\Delta x_I - L_1\left[1-\cos(\theta_{eq}/2)\right]\right\} - 2\int_V \frac{1}{2}EI\kappa^2 dV - 2\int_L \frac{1}{2}E\varepsilon^2 dx \quad \text{(S-4)}$$

To enable energy saving through snap-through bistability, the energy barrier ΔE of the bistable actuator must satisfy:

$$\Delta E < E_{input} < U_{actuator,II} \quad \text{(S-5)}$$

where E_{input} is the energy consumption of the system and $U_{actuator,II}$ is the strain energy of the soft actuators at rest states (or at stopping angle). This equation can be easily simplified as:

$$\frac{1}{2}k\{2\Delta x_I - L_1[1-\cos(\theta_s/2)]\}L_1[1-\cos(\theta_s/2)] < 2U_{actuator,II} \quad \text{(S-6)}$$

θ_s is the stop angle. $U_{actuator,II}$ can be approximately obtained as:

$$U_{actuator,II} = 2\int_L \frac{1}{2}EI\kappa^2 dx + 2\int_V \frac{1}{2}E\varepsilon^2 dV \quad \text{(S-7)}$$

where $\kappa \approx 2\tan\left(\theta_l/2\right)/L$ is the approximate curvature in the soft actuator. $\varepsilon \approx 1-\theta_s/\left[2\tan(\theta_s/2)\right]$ is the approximate strain in the soft actuator.

From Eq. (S-5), we see that when the spring stiffness or extension is relatively small, the bistable hybrid actuator costs less energy than its soft counterparts to achieve the same bending angle. When the spring stiffness or pretension is set to be too large, it will readily satisfy Eq. (S-5). In this case, the bistable actuator will require more energy input than its soft counterpart to achieve the same bending angle. However, the benefit of the bistable actuator with a high-stiffness spring is that it yields a much higher force output than the entirely soft actuator. Therefore, a trade-off in selecting spring stiffness should be considered for different conditions (more energy saving or larger force output).

3. Static Blocking Force of a Bistable Rigid Linkage through Quasi-Static Indentation

An indentation test is performed to characterize the reaction force profile of the bistable rigid linkages alone, as shown in the inset of Fig. S5A. We also build a model to predict the indentation force F_{indent} as a function of indentation distance δ:

$$F_{indent} = \frac{k \triangle x_{II} L_1 \sin[\frac{1}{2}\arcsin(\frac{-2\delta + L\sin(\theta_s)}{L})]}{L\sqrt{1-[\frac{-2\delta + L\sin(\theta_s)}{L}]^2}} \tag{S-8}$$

where Δx_{II} represents the spring extension at rest state (State II). In this equation, we assume free rotation of the joint, thus the rest state of the linkages is at the stop angle regardless of spring stiffness. In both experiment and model, we use L = 70 mm, L_1 = 23.33 mm and θ_s = 60°. Fig. S5B shows that the experimental result agrees very well with the model. Both results show that, at the rest state of stopping angle, it requires the maximum force to deform the linkages, and at planar state, the loading force decreases to 0. Further indentation beyond planar state results in the snap through of the rigid linkages towards another rest state.

4. Modeling of Static Blocking Force of the BH-SBA

Here we build a model to predict the static end-effector reaction force of the bistable hybrid soft actuator under non-actuated state (no pressurization applied). Based on the total potential energy of the system, U, in Eq. (S-2), the joint torque, T, of the bistable actuator can be obtained by

$$T = \frac{dU}{d\theta} \tag{S-9}$$

With Eq. (S-9), we can plot the joint torque of BH-SBA vs. spring pretension, Δx_I, and bending angle, θ, as shown in Fig. S4B.

The static blocking force of the system, f_b , or the reaction force of the end-effector, can be obtained by

$$f_b = \frac{T}{\frac{L}{2}\cos(\theta)} \tag{S-10}$$

Based on this equation, we plot the static blocking force as a function of spring pretension, Δx_I, and bending angle, θ, as shown in Fig. S4A.

From both Fig. S4A and Fig. S4B, we observe that the static blocking force (or joint torque) of the bistable actuator is linearly proportional to the spring pretension length under the same bending angle. It shows that the static force output of the bistable actuator can be tuned by simply varying the spring pretension, where an increase in spring pretension can improve the static force exertion of the hybrid system.

Despite the linearity along the spring pretension axis, the static force (or joint torque) shows a nonlinear relationship with the bending angle. This nonlinear relationship is more clearly shown in Fig. S4C, where we observe that BH-SBA generates its maximum static force at neither $\theta = \theta_s$

(here we use $\theta_s = 60^o$) nor $\theta = 0^o$, but somewhere between these two bounds. This maximum value can be obtained by satisfying $dF_b/d\theta = 0$. The nonlinear relationship in Figure S4C is validated by the experiment results shown in Fig. S4D, where we performed an indentation test using Instron to capture the static force output (no pressurization).

For the case of high-stiffness springs (e.g. in the bistable hybrid soft gripper), since the high-stiffness spring could generate much higher potential energy than the straining energy of the soft actuators alone at the resting state, the effect of the soft bending actuators on determining the static blocking force of the bistable hybrid soft actuator can be neglected at the resting state (this assumption is not valid in other unstable states). This assumption explains the minor discrepancy between the model and experimental results in predicting the block force. In this case, the static blocking force of the bistable actuator in Eq. (S-10) shown in Fig. 6B can be further simplified as:

$$f_b \approx \frac{k(\triangle x_{II} + \triangle x)\sin\left(\theta_s/2\right)}{\cos(\theta_s)}\frac{L_1}{L} \tag{S-11}$$

5. Finite Element Method Simulation on Actuating Bistability of the BH-SBA

The Finite Element Method (FEM) simulation is couducted using ABAQUS/Standard (Simulia, Dassault Systems, 6.14). Only half of the hybrid soft bending actuator model is simulated due to the symmetry of its geometry. The geometry and material property parameters can be found in Table S1. The pneumatic soft bending actuator is modeled with 3D solid elements (C3D8RH) and the hyperelastic Yeoh model (C_{10} = 0.019 MPa, C_{20} = 0.0009 MPa, C_{30} = - 4.75 $\times$ 10^{-6} MPa, $D_1 = D_2 = D_3 = 0$ for the SI (mm) unit system) (*50*) is used to simulate the constitutive behavior of the Ecoflex-50. The rigid linkage is modeled with 2D shell elements (S3 and S4R), and isotropic, linear elastic model is used to simulate the constitutive behavior of the spine made of PLA with Young's modulus of 3.5 GPa and Poisson's ratio of 0.33.A hinge connection is used to simulate the revolute joint that connects the two spines. To simulate the mechanical angle stoppers on two sides, we add a stop behavior to the hing by specifying the stop angles. A damping coefficient (0.1) is also added to prevent the bouncing of the spine after collision with the stopper. A tie interaction is used to attach the linkages and the actuator together. In the bistable linkages, the spring is modeled with an axial connector element (CONN3D2) and attached to the rigid links using a kinematic coupling. A reference length is set to simulate the pretension in the spring. The model contains a total of 19,015 elements. For the boundary condition, the bottom of the spine is fixed, and a symmetrical boundary condition is applied to nodes at the middle of the mechanism. There are 3 steps beside the initial step to simulate the motion of a bistable bending actuator. First, a static step is used to apply a rotational displacement to rotate the mechanism to - 60^o. This step is necessary, since the system is initially at perfect vertical angle and cannot move without a pertubance though the sping's pretension force is applied. Second, a static step is followed to allow the actuator and the mechanism to reach a steady state, which allows the mechanism to stay at a stable angle (- 60^{o}) after the release of the pretensioned spring. Third, a full dynamic step analysis applies a smooth step pressure to actuate the pneumatic actuator. To capture the snap-through, the minimum time step size is set as 1×10^{-8} s that ensures the convergence of the simulation. All the three steps use a direct, full Newton solver.

Figures

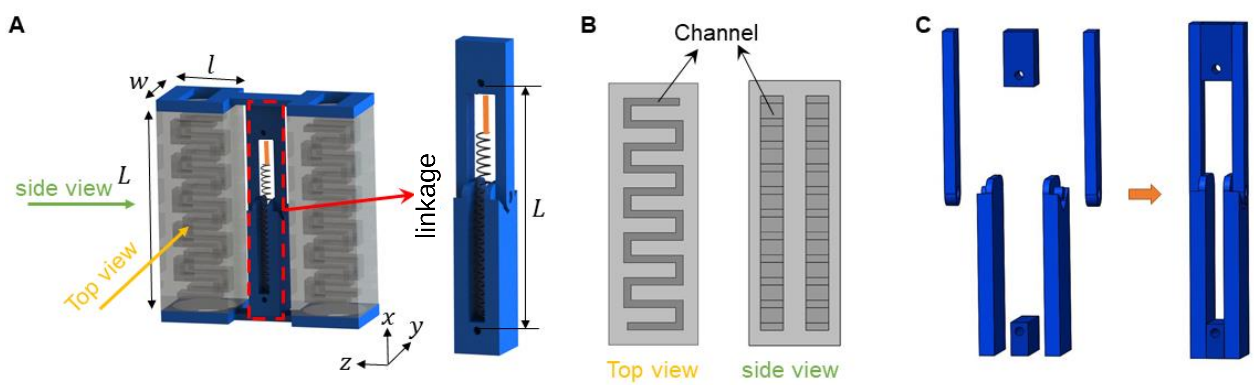

Fig. S1. Structure of the bistable hybrid soft bending actuator (BH-SBA). (A) Schematic of BH-SBA. It is composed of two pneumatic actuators, one rotation spine and one pretensioned spring. (B) Schematics of top view (left) and side view (right) of the two-way pneumatic bending actuator. The darker color represents the patterned channel. (C) Exploded schematics of the structure of the 3d-printed linkages for BH-SBA.

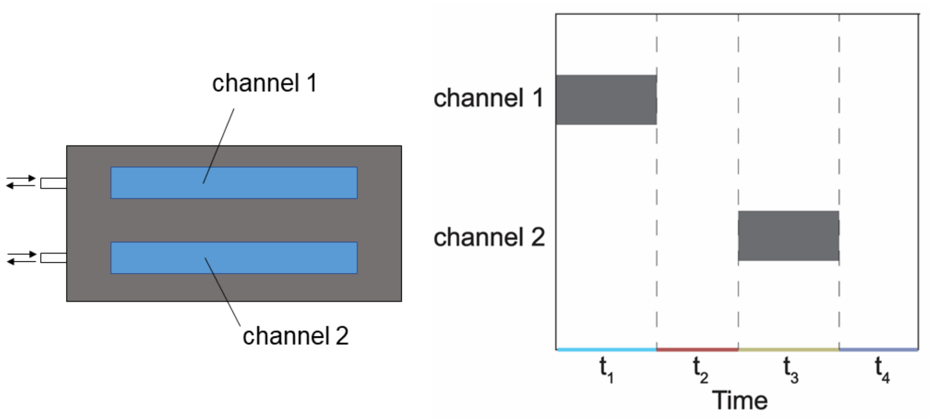

Fig. S2. Actuation timing control for the BH-SBAs. The grey lines in the right figure shows when a channel is pressurized. At all other times, channels are not actuated. The detailed data for controlling the proposed actuators and machines can be found in Table. S2.

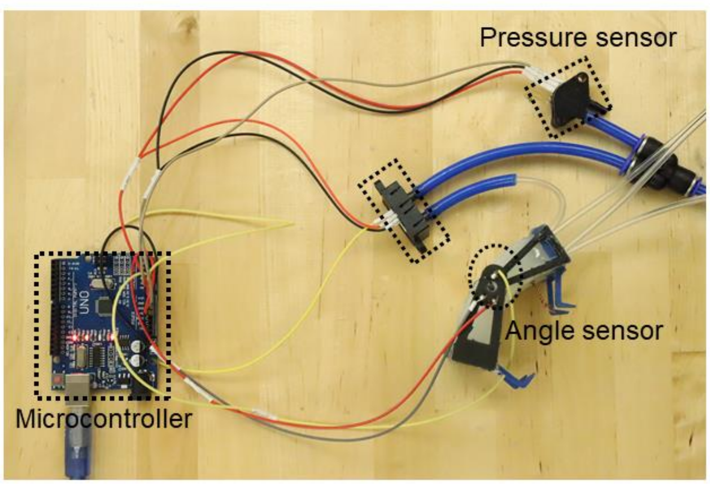

Fig. S3. Experimental setup for the measurement of bending angle, pressure, and flow rate for the bistable actuator. (Photo Credit: Yinding Chi, North Carolina State University)

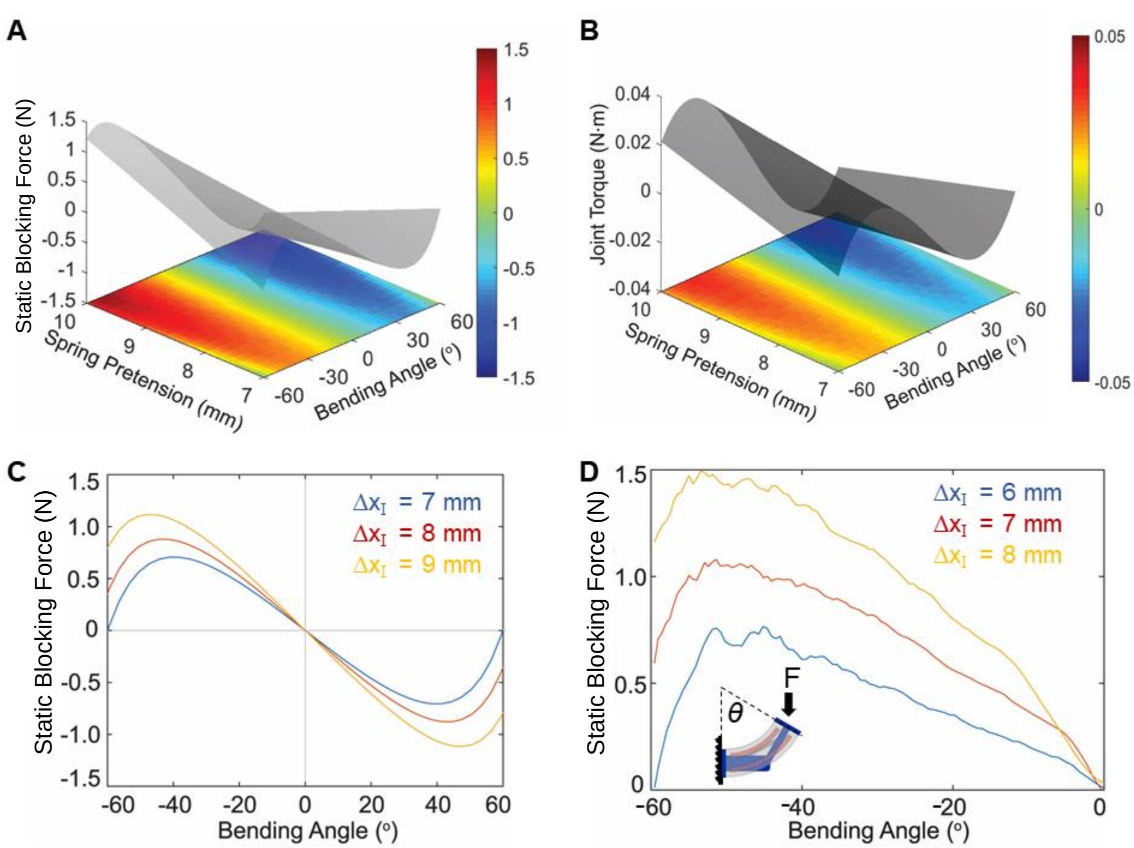

Fig. S4. Static blocking force and joint torque of the BH-SBA. (A) Theoretical static blocking force vs. spring pretension at state I, Δx_I, and bending angle, θ. We use spring stiffness k = 1.29 N/mm. (B) Theoretical joint torque vs. spring pretension at state I, Δx_I, and bending angle, θ. (C) Theoretical static blocking force as the function of bending angle. (D) Static blocking force as the function of bending angle measured by indenting test, further indenting beyond 0^o results in a snap-through. The inset shows the set-up of the experiment, where we used Instron to capture the force.

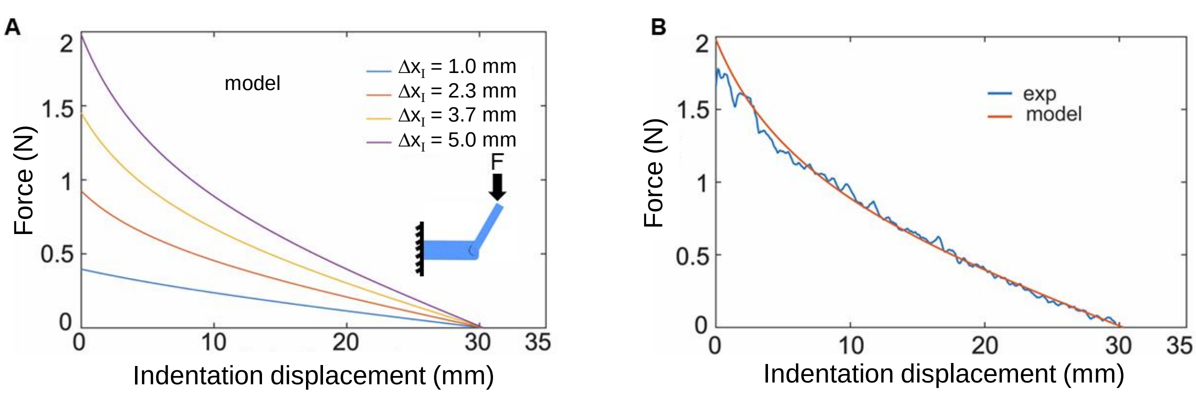

Fig. S5. Force-displacement curves of the sole bistable linkages of BH-SBA under quasi-static indentation. (A) the theoretical force-displacement curves for sole spines with different spring pre-extensions (Δx_I). The spring stiffness k = 1.29 N/mm. Further displacement beyond

~30 mm results in a snap-through. (B) Comparison of the theoretical model with the experimental result, which shows a good match (Δx_I = 5.0mm).

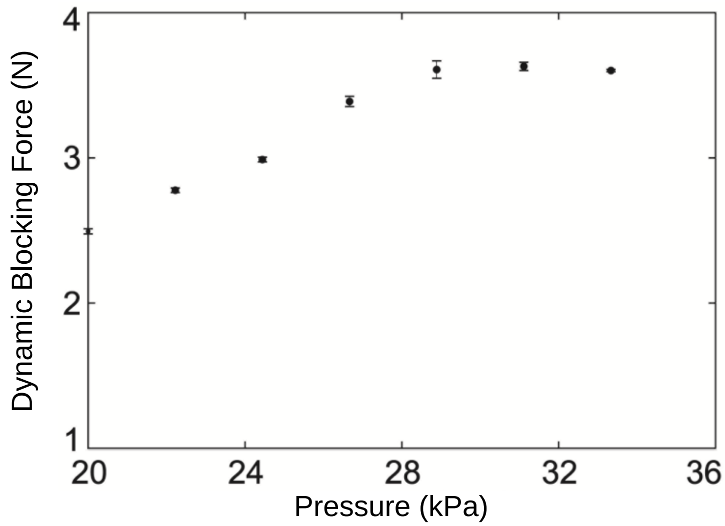

Fig. S6. Dynamic blocking force of the BH-SBA vs. input pressure. The force, at the bending angle of ~28^o, is captured during the swing motion of the actuator (k = 1.29 N/mm, Δx_I = 6mm).

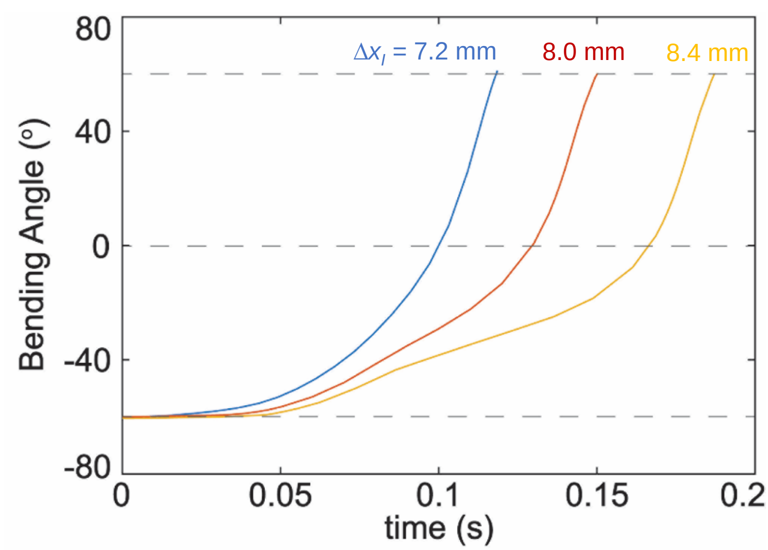

Fig. S7. The simulated bending angle vs. response time for the BH-SBAs with different spring pretensions (Δx_I = 7.2 mm, 8 mm and 8.4 mm, respectively)**.** Here all BH-SBAs possess the same lock angle 60^o and are actuated with 40 kPa instantaneous pressure. The detailed time elapse can be found in Table. S3.

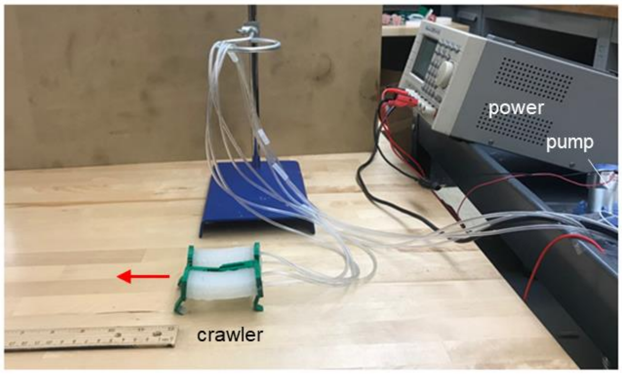

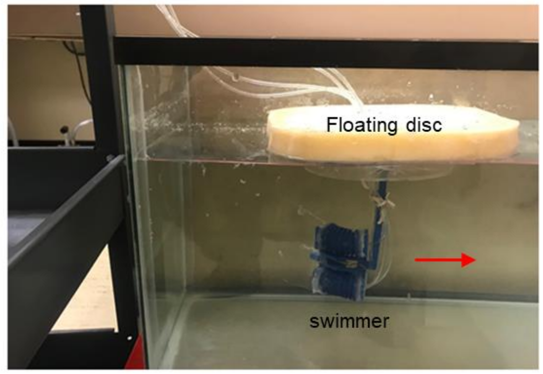

Fig. S8. Experimental setup of the soft robotics crawler (left) and soft robotic swimmer (right). All three types of robotic swimmers (bistable hybrid soft, hybrid, and soft ones are connected with a lightweight floating disc (yellow) on the top to avoid the influence of buoyancy changes. (Photo Credit: Yichao Tang, Temple University)

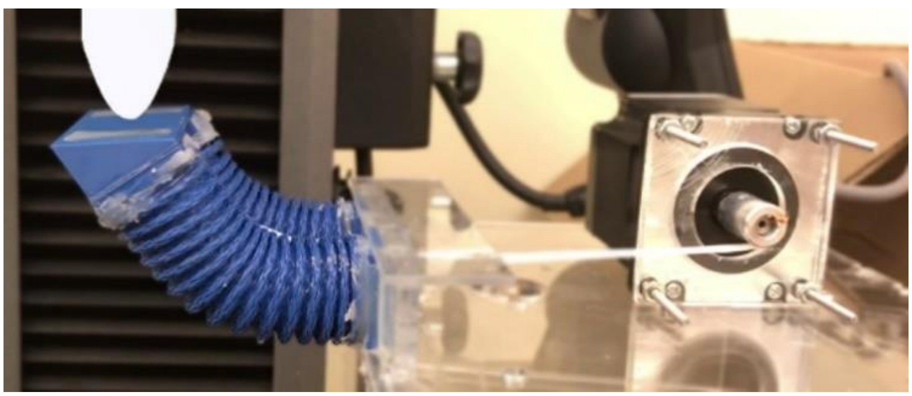

Fig. S9. Experimental setup of bending stiffness measurements. The force (blocked at 80^o) is recorded by an Instron machine while the motor (AutomationDirect, Inc.) is pulling the spring at a rate of 5 revolutions per minute (RPM). (Photo Credit: Yichao Tang, Temple University)

Table. S1. List of geometrical and materials parameters for the BH-SBA

Parameter	Symbol	Value	Unit
Ecoflex – 50 Nominal Young's modulus	E	35	kPa
Ecoflex – 50 Density	ρ	1×10^{-9}	t/mm^3
length of soft actuator	L	70	mm
cross-section dimension of channel	$w_c \times h$	2 x 6	mm
cross-section dimension of soft actuator	$w \times l$	14 x 20	mm
distance between anchor points	L_1	23.3	mm
spring pretension at state I	Δx_I	-	mm
volume of soft actuator	$V=wlL$	1.96×10^{-5}	m^3
spring stiffness	k	1.29	N/mm
second moment of inertia	$I=w^3l/12$	4.57×10^{-9}	m^4
peak power (BH-SBA Fig.3B)	-	8.0	W
stored energy/weight (BH-SBA Fig.3B)	-	1.156	J/kg

Table. S2. Data of actuation pressure and time control pattern. The actuation timing control is shown in Fig. S2.

Actuators / robots	P (kPa)	t_1 (s)	t_2 (s)	t_3 (s)	t_4 (s)
BH-SBA (Fig. 3A-3C)	20	0.09	0.07	0.09	0.07
crawler (Fig. 4C)	20	0.09	0.07	0.09	0.07
crawler (Fig. 4D)	30	0.11	0.08	0.11	0.08
swimmer (Fig. 5)	160	0.15	0.23	0.15	0.23

Table. S3. The time elapse of the SBA, H-SBA, and BH-SBAs with different spring pretensions. All actuators are pressurized at 30 kPa with the same flow rate of ~3 L/min

	Time before snap-through (s)	Time after snap-through (s)
BH-SBA (Δx_I = 3.1 mm)	0.262 (-41^o to 0)	0.063 (0 to 41^o)
BH-SBA (Δx_I = 6 mm)	0.763 (-60^o to 0)	0.065 (0 to 60^o)
BH-SBA (Δx_I = 7 mm)	0.790 (-60^o to 0)	0.062 (0 to 60^o)
BH-SBA (Δx_I = 8 mm)	0.979 (-60^o to 0)	0.053 (0 to 60^o)
SBA	1.261 (0 to 60^o)	N.A.
H-SBA	2.600 (0 to 25.3^o)	N.A.

Table. S4. The simulated time elapse of the BH-SBAs with different spring pretensions.

Δx_I	time before snap (s)	time after snap (s)
7.2 mm	~0.099	~0.033
8.0 mm	~0.128	~0.032
8.4 mm	~0.164	~0.030

Movie captions:

Movie S1. Slow motion of swinging of the bistable hybrid soft bending actuator (BH-SBA) captured by a high-speed camera. The actuator is pressurized at 20 kPa and 3.2 Hz average frequency.

Movie S2. Comparison of the real-time swing motion between the BH-SBA and its two counterparts, hybrid soft bending actuator (H-SBA), and soft bending actuator (SBA) with the same swing angle of 60^o. When pressurized at 20 kPa, it takes BH-SBA 0.13 s to swing from -60^o to 60^o (average frequency = 3.85 Hz). It takes SBA 0.16 s (need to be pressurized at 38 kPa) to achieve the same bending angle. The H-SBA requires the highest pressure (80 kPa) to achieve the same bending angle at the slowest speed (0.27 s).

Movie S3. FEM simulation on actuating the bistability of the BH-SBAs with different spring pretensions (Δx_I = 7.2 mm, 8 mm and 8.4 mm, respectively)**.** All actuators rest at the preset stopping angle of 60^o and are then actuated with an applied 40 kPa instantaneous pressure. In the simulation, we use the same geometry, material and spring properties as the experiment.

Movie S4. Comparison of the real-time locomotion on a horizontal surface between the three crawlers based on the integrated BH-SBA, H-SBA, and SBA. All actuators are pressured at 20 kPa with a 3.2 Hz average frequency. All crawlers are 7 cm long and 6 cm wide with a mass of 45g. The prototype built with BH-SBA shows the fastest locomotion speed (2.49 BL/s or 174.4 mm/s). The crawler based on springless H-SBA shows the slowest velocity (0.53 BL/s or 37.1 mm/s). The crawler based on SBA without linkages can achieve locomotion at 1.19 BL/s, or 83.3 mm/s.

Movie S5. Slow motion (x 0.125) of the BH-SBA-based crawler locomoting on a horizontal surface. Due to the amplified force and velocity enabled by the bistable structure, we observe the lift-off of both foreleg and hind legs from the surface during the locomotion.

Movie S6. Comparison of the real-time locomotion of three BH-SBA-based crawlers on a horizontal surface with different spring pretension. All actuators are pressured at 30 kPa with a 2.63 Hz average frequency. All crawlers are 7 cm long and 6 cm wide with a mass of 45g. The prototype built with largest spring pretension (Δx_I = 8 mm) shows the fastest locomotion speed (2.68 BL/s or 187.5 mm/s). The crawler with Δx_I = 6 mm shows the slowest velocity (1.93 BL/s or 135.1 mm/s). The crawler with Δx_I = 7 mm can achieve locomotion at 2.26 BL/s, or 157.6 mm/s.

Movie S7. Comparison of the real-time climbing on a slightly tilted surface between the three crawlers based on the integrated BH-SBA, H-SBA, and SBA. All actuators are pressurized at 20 kPa with a 3.2 Hz average frequency. The crawler built with BH-SBA can locomote on a 17^o tilted surface with a 0.56 BL/s locomotion velocity while the crawlers based on SBA and H-SBA do not show the capability of climbing such surfaces.

Movie S8. Comparison of the real-time underwater locomotion between the three fish-like swimmers based on the integrated BH-SBA, H-SBA, and SBA. The prototype is ~150 mm long with a mass of 51 g. The composed bending actuator is 45 mm in length and 25 mm in diameter. We use a stiff plastic film (0.25 mm) for the fish fin. The prototype built with BH-SBA can locomote at 0.78 BL/s, or 117 mm/s. The crawler based on springless H-SBA shows the slowest velocity (0.27 BL/s or 40 mm/s). The crawler based on SBA can achieve a locomotion speed of 0.58 BL/s, or 87 mm/s.

Movie S9. Demonstrations of strength-adjustable bistable hybrid soft grippers in grasping a variety of objects ranging from fragile lightweight to high-load objects. Pneumatic actuation is used for gripping lightweight and fragile objects and motor-driven actuation is used for grasping large and heavy objects through pulling the spring. We first show the proposed gripper can manipulate a few lightweight objects including a fresh egg, steel wrap, a glass bottle and a tape. All actuators are pressurized at 90 kPa. Then we demonstrate the proposed gripper can hold heavier objects with weights of 600 g, 3.6 kg, 9.2 kg and 11.4 kg. The corresponding stretched lengths of the spring (k = 9.7 N/mm) at stop angle of 85^o are ~0.1 mm, ~3 mm, ~2 mm and ~3 mm. For the demonstration of grasping 9.2 kg and 11.4 kg payloads, an acrylic plate is fixed above the payload. Gripping these payloads is achieved through squeezing the acrylics plate first and then lifting the payloads.

REFERENCES AND NOTES

1. R. F. Shepherd, F. Ilievski, W. Choi, S. A. Morin, A. A. Stokes, A. D. Mazzeo, X. Chen, M. Wang, G. M. Whitesides, Multigait soft robot. *Proc. Natl. Acad. Sci. U.S.A.* **108**, 20400–20403 (2011).

2. R. Deimel, O. Brock, A novel type of compliant and underactuated robotic hand for dexterous grasping. *Int. J. Robot. Res.* **35**, 161–185 (2016).

3. P. Polygerinos, Z. Wang, K. C. Galloway, R. J. Wood, C. J. Walsh, Soft robotic glove for combined assistance and at-home rehabilitation. *Robot. Auton. Syst.* **73**, 135–143 (2015).

4. E. W. Hawkes, L. H. Blumenschein, J. D. Greer, A. M. Okamura, A soft robot that navigates its environment through growth. *Sci. Robot.* **2**, eaan3028 (2017).

5. A. D. Marchese, R. Tedrake, D. Rus, Dynamics and trajectory optimization for a soft spatial fluidic elastomer manipulator. *Int. J. Robot. Res.* **35**, 1000–1019 (2016).

6. R. V. Martinez, J. L. Branch, C. R. Fish, L. Jin, R. F. Shepherd, R. M. D. Nunes, Z. Suo, G. M. Whitesides, Robotic tentacles with three-dimensional mobility based on flexible elastomers. *Adv. Mater.* **25**, 205–212 (2013).

7. M. A. Robertson, J. Paik, New soft robots really suck: Vacuum-powered systems empower diverse capabilities. *Sci. Robot.* **2**, eaan6357 (2017).

8. K. Jayaram, R. J. Full, Cockroaches traverse crevices, crawl rapidly in confined spaces, and inspire a soft, legged robot. *Proc. Natl. Acad. Sci. U.S.A.* **113**, E950–E957 (2016).

9. P. Glick, S. Suresh, D. Ruffatto, M. Cutkosky, M. T. Tolley, A. Parness, A soft robotic gripper with gecko-inspired adhesive. *IEEE Robot. Autom. Lett.* **3**, 903–910 (2018).

10. D. Yang, M. S. Verma, J.-H. So, B. Mosadegh, C. Keplinger, B. Lee, F. Khashai, E. Lossner, Z. Suo, G. M. Whitesides, Buckling pneumatic linear actuators inspired by muscle. *Adv. Mater. Technol.* **1**, 1600055 (2016).

11. A. T. Baisch, O. Ozcan, B. Goldberg, D. Ithier, R. J. Wood, High speed locomotion for a quadrupedal microrobot. *Int. J. Robot. Res.* **33**, 1063–1082 (2014).

12. R. M. Alexander, N. J. Dimery, R. F. Ker, Elastic structures in the back and their rôle in galloping in some mammals. *J. Zool.* **207**, 467–482 (1985).

13. M. Hildebrand, Motions of the running cheetah and horse. *J. Mammal.* **40**, 481–495 (1959).

14. P. Eckert, A. Spröwitz, H. Witte, A. J. Ijspeert, Comparing the effect of different spine and leg designs for a small bounding quadruped robot, in *2015 IEEE International Conference on Robotics and Automation (ICRA)* (IEEE, 2015), pp. 3128–3133.

15. Q. Zhao, B. Ellenberger, H. Sumioka, T. Sandy, R. Pfeifer, The effect of spine actuation and stiffness on a pneumatically-driven quadruped robot for cheetah-like locomotion, in *2013 IEEE International Conference on Robotics and Biomimetics (ROBIO)* (IEEE, 2013), pp. 1807–1812.

16. J. Duperret, D. E. Koditschek, Empirical validation of a spined sagittal-plane quadrupedal model, in *2017 IEEE International Conference on Robotics and Automation (ICRA)* (IEEE, 2017), pp. 1058–1064.

17. T. Chen, O. R. Bilal, K. Shea, C. Daraio, Harnessing bistability for directional propulsion of soft, untethered robots. *Proc. Natl. Acad. Sci. U.S.A.* **115**, 5698–5702, (2018).

18. P. Rothemund, A. Ainla, L. Belding, D. J. Preston, S. Kurihara, Z. Suo, G. M. Whitesides, A soft, bistable valve for autonomous control of soft actuators. *Sci. Robot.* **3**, eaar7986 (2018).

19. J. T. B. Overvelde, T. Kloek, J. J. A. D'haen, K. Bertoldi, Amplifying the response of soft actuators by harnessing snap-through instabilities. *Proc. Natl. Acad. Sci. U.S.A.* **112**, 10863–10868 (2015).

20. J.-S. Koh, E. Yang, G.-P. Jung, S.-P. Jung, J. H. Son, S.-I. Lee, P. G. Jablonski, R. J. Wood, H.-Y. Kim, K.-J. Cho, Jumping on water: Surface tension–dominated jumping of water striders and robotic insects. *Science* **349**, 517–521 (2015).

21. S.-P. Jung, G.-P. Jung, J.-S. Koh, D.-Y. Lee, K.-J. Cho, Fabrication of composite and sheet metal laminated bistable jumping mechanism. *J. Mech. Robot.* **7**, 021010 (2015).

22. M. Noh, S.-W. Kim, S. An, J.-S. Koh, K.-J. Cho, Flea-inspired catapult mechanism for miniature jumping robots. *IEEE Trans. Robot.* **28**, 1007–1018 (2012).

23. B. Vanderborght, A. Albu-Schäffer, A. Bicchi, E. Burdet, D. G. Caldwell, R. Carloni, M. Catalano, O. Eiberger, W. Friedl, G. Ganesh, M. Garabini, M. Grebenstein, G. Grioli, S. Haddadin, H. Hoppner, A. Jafari, M. Laffranchi, D. Lefeber, F. Petit, S. Stramigioli, N. Tsagarakis, M. Van Damme, R. Van Ham, L. C. Visser, S. Wolf, Variable impedance actuators: A review. *Robot. Auton. Syst.* **61**, 1601–1614 (2013).

24. B. Shin, J. Ha, M. Lee, K. Park, G. H. Park, T. H. Choi, K.-J. Cho, H.-Y. Kim, Hygrobot: A self-locomotive ratcheted actuator powered by environmental humidity. *Sci. Robot.* **3**, eaar2629 (2018).

25. Y. Tang, Q. Zhang, G. Lin, J. Yin, Switchable adhesion actuator for amphibious climbing soft robot. *Soft Robot.* **5**, 592–600 (2018).

26. S. Seok, C. D. Onal, K.-J. Cho, R. J. Wood, D. Rus, S. Kim, Meshworm: A peristaltic soft robot with antagonistic nickel titanium coil actuators. *IEEE/ASME Trans. Mech.* **18**, 1485–1497 (2013).

27. T. Umedachi, V. Vikas, B. Trimmer, Softworms: The design and control of non-pneumatic, 3D-printed, deformable robots. *Bioinspir. Biomim.* **11**, 025001 (2016).

28. C. D. Onal, D. Rus, Autonomous undulatory serpentine locomotion utilizing body dynamics of a fluidic soft robot. *Bioinspir. Biomim.* **8**, 026003 (2013).

29. J. Cao, L. Qin, J. Liu, Q. Ren, C. C. Foo, H. Wang, H. P. Lee, J. Zhu, Untethered soft robot capable of stable locomotion using soft electrostatic actuators. *Extreme Mech. Lett.* **21**, 9–16 (2018).

30. W.-B. Li, W.-M. Zhang, H.-X. Zou, Z. Peng, G. Meng, A fast rolling soft robot driven by dielectric elastomer. *IEEE/ASME Trans. Mech.* **23**, 1630–1640 (2018).

31. M. Duduta, D. R. Clarke, R. J. Wood, A high speed soft robot based on dielectric elastomer actuators, in *2017 IEEE International Conference on Robotics and Automation (ICRA)* (IEEE, 2017), pp. 4346–4351.

32. X. Huang, K. Kumar, M. K. Jawed, A. M. Nasab, Z. Ye, W. Shan, C. Majidi, Chasing biomimetic locomotion speeds: Creating untethered soft robots with shape memory alloy actuators. *Sci. Robot.* **3**, eaau7557 (2018).

33. T. Park, Y. Cha, Soft mobile robot inspired by animal-like running motion. *Sci. Rep.* **9**, 14700 (2019).

34. M. Cianchetti, T. Ranzani, G. Gerboni, I. De Falco, C. Laschi, A. Menciassi, STIFF-FLOP surgical manipulator: Mechanical design and experimental characterization of the single module, in *2013 IEEE/RSJ International Conference on Intelligent Robots and Systems (IROS)* (IEEE, 2013), pp. 3576–3581.

35. F. G. Serchi, A. Arienti, C. Laschi, Biomimetic vortex propulsion: Toward the new paradigm of soft unmanned underwater vehicles. *IEEE/ASME Trans. Mech.* **18**, 484–493 (2013).

36. S.-H. Song, M.-S. Kim, H. Rodrigue, J.-Y. Lee, J.-E. Shim, M.-C. Kim, W.-S. Chu, S.-H. Ahn, Turtle mimetic soft robot with two swimming gaits. *Bioinspir. Biomim.* **11**, 036010 (2016).

37. T. Li, G. Li, Y. Liang, T. Cheng, J. Dai, X. Yang, B. Liu, Z. Zeng, Z. Huang, Y. Luo, T. Xie, W. Yang, Fast-moving soft electronic fish. *Sci. Adv.* **3**, e1602045 (2017).

38. M. D. Bartlett, N. Kazem, M. J. Powell-Palm, X. Huang, W. Sun, J. A. Malen, C. Majidi, High thermal conductivity in soft elastomers with elongated liquid metal inclusions. *Proc. Natl. Acad. Sci. U.S.A.* **114**, 2143–2148 (2017).

39. J. Najem, S. A. Sarles, B. Akle, D. J. Leo, Biomimetic jellyfish-inspired underwater vehicle actuated by ionic polymer metal composite actuators. *Smart Mater. Struct.* **21**, 094026 (2012).

40. H. Jin, E. Dong, G. Alici, S. Mao, X. Min, C. Liu, K. L. Low, J. Yang, A starfish robot based on soft and smart modular structure (SMS) actuated by SMA wires. *Bioinspir. Biomim.* **11**, 056012 (2016).

41. R. K. Katzschmann, J. DelPreto, R. MacCurdy, D. Rus, Exploration of underwater life with an acoustically controlled soft robotic fish. *Sci. Robot.* **3**, eaar3449 (2018).

42. Y. Yang, Y. Chen, Novel design and 3D printing of variable stiffness robotic fingers based on shape memory polymer, in *2016 6th IEEE International Conference on Biomedical Robotics and Biomechatronics (BioRob)* (IEEE, 2016), pp. 195–200.

43. M. Manti, T. Hassan, G. Passetti, N. D'Elia, C. Laschi, M. Cianchetti, A bioinspired soft robotic gripper for adaptable and effective grasping. *Soft Robot.* **2**, 107–116 (2015).

44. M. Manti, V. Cacucciolo, M. Cianchetti, Stiffening in soft robotics: A review of the state of the art. *IEEE Robot. Autom. Mag.* **23**, 93–106 (2016).

45. S. Mintchev, J. Shintake, D. Floreano, Bioinspired dual-stiffness origami. *Sci. Robot.* **3**, eaau0275 (2018).

46. J. A. Faber, A. F. Arrieta, A. R. Studart, Bioinspired spring origami. *Science* **359**, 1386–1391 (2018).

47. S.-W. Kim, J.-S. Koh, J.-G. Lee, J. Ryu, M. Cho, K.-J. Cho, Flytrap-inspired robot using structurally integrated actuation based on bistability and a developable surface. *Bioinspir. Biomim.* **9**, 036004 (2014).

48. B. Mosadegh, P. Polygerinos, C. Keplinger, S. Wennstedt, R. F. Shepherd, U. Gupta, J. Shim, K. Bertoldi, C. J. Walsh, G. M. Whitesides, Pneumatic networks for soft robotics that actuate rapidly. *Adv. Funct. Mater.* **24**, 2163–2170 (2014).

49. O. H. Maghsoudi, A. Vahedipour, B. Robertson, A. Spence, Application of superpixels to segment several landmarks in running rodents. *Pattern Recogn. Image Anal.* **28**, 468–482 (2018).

50. P. Kulkarni, "Centrifugal forming and mechanical properties of silicone-based elastomers for soft robotic actuators," thesis, Rutgers The State University of New Jersey, New Brunswick (2015)